Supplementary Information

Cross-Linked Curcumin/Kaolin Composite and A Mathematical Model-Validated Method for Comprehensive Fingerprint Imaging

Jiujiang Wang [a], Dawu Li [a,*], Jianghua Zhang [b], Zijian Gao [c], Jinke Han [d]

[a] Key Laboratory of Impression Evidence Examination and Identification Technology, Ministry of Public Security, College of Forensic Science, Criminal Investigation Police University of China, Shenyang, Liaoning, 110854, China

[b] Key Laboratory of Anti-Drug Technology of Liaoning Provincial, College of Anti-Drug and Public Security, Criminal Investigation Police University of China, Shenyang, Liaoning, 110854, China

[c] Department of Information Systems, Business Statistics and Operations Management, HKUST Business School, The Hong Kong University of Science and Technology, Hong Kong, 999077, China

[d] Questrom School of Business, Boston University, Boston, MA, 02215, USA

Corresponding Author:

Dawu Li

Email: Ldw20001980@163.com

Content

1. Experimental Section

1.1. Design Strategy.

Chemical techniques for the visualization of LFPs produce images of friction ridges of the fingerprint through interaction between the residues of LFPs left on substrates and the chemical reagent [1]. Herein, we reasoned that the strong adsorptivity of kaolin would facilitate adhesion with the fingerprint residues [2]. Meanwhile, using a large amount of kaolin to load trace amounts of curcumin would reduce costs and overcome the ACQ effect of bare curcumin to maintain stable fluorescence. Furthermore, we deduced that H-bonds shall be formed between curcumin and kaolin and the physical crosslinking between curcumin and kaolin will be enhanced [3]. Curcumin is a phenolic antioxidant and diketone compound with unsaturated aliphatic and aromatic groups in its main chain [4]. Being widely used as the cross-linker and carrier material, kaolin is a layered silicate with the crystal structure composed of Si-centered tetrahedra and Al-centered octahedra (1:1 type mineral), and a considerable number of active hydroxyl groups exist in its interlayer and surface [5, 6]. When dried at 90℃, kaolin undergoes substantial water loss, resulting in that the particle spacing is reduced and the curcumin particles can be adsorbed both within and on the surface of its layered structure. Additionally, hydrogen bonds can be formed between curcumin and kaolin, and thereby the interaction between curcumin and kaolin will be enhanced, resulting in robust adsorption of curcumin on the surface of kaolin and the formation of a stable complex between them. Being excited by 365nm, the as-prepared curcumin/kaolin powders display yellow-green and green fluorescence.

1.2. Instrumentation and Characterization.

The morphology, particle size, distribution, and atomic composition of the curcumin/kaolin composites were observed using a scanning electron microscope (SEM) (Shimadzu, SS-550) equipped with an energy dispersive spectroscope (EDS). An X-ray fluorescence spectrometer (Marvern Panalytical, Zetium) was employed to conduct X-ray fluorescence spectroscopy (XRF) to determine the chemical composition and content of kaolin. Crystallographic information was obtained using X-ray diffraction (XRD) using an X-ray diffractometer (Bruke, D8 ADVANCE). Chemical states of C, O, Si, and Al elements that exist within the synthesized composites were analyzed by X-ray photoelectron spectroscopy (XPS) using an X-ray photoelectron spectrometer (Thermo Scientific, K-Alpha). The Fourier transform infrared (FT-IR) spectra were collected using an FTIR spectrometer (Shimadzu, IRTracer-100) via the standard KBr disk method. Raman spectra of the kaolin and curcumin/kaolin composites were recorded using a Raman spectrometer (HORIBA Scientific, XploRA plus) with a laser wavelength of 785 nm. Ultraviolet−visible (UV−vis) absorption spectra and fluorescence spectra of curcumin and curcumin/kaolin composite powders were recorded using a UV−vis spectrophotometer (Hitach, UH4100) and a fluorescence spectrophotometer (Hitach, F-7000), respectively. Quantum yields of the curcumin/kaolin composite powders (365nm) were measured using a photoluminescence spectrophotometer (Edinburgh FLS980).

1.3. Operation Process of FFIR.

ImageJ software was used to conduct this experiment. Specifically, the images of LFPs were first converted into 8-bit grayscale images using the Type-8-bit tool. Then, the Threshold tool was

employed to select the areas of fingerprint and background based on the gray threshold, and the mean gray values of images of LFPs were measured using the Analyze-Measure tool.

Program S1. Fingerprint signal selection and fluorescence intensity determination based on adaptive grayscale thresholding.

```
run("8-bit");
set Auto Threshold ("Default no-reset");
//run ("Threshold...");
ret Auto Threshold ("Default dark no-reset");
run ("Set Measurements...", "area mean min integrated limit redirect=None decimal=3");
run("Measure");
```

Program S2. Background noise selection and fluorescence intensity determination based on adaptive grayscale thresholding.

```
run("8-bit");
set Auto Threshold ("Default dark no-reset");
//run ("Threshold...");
set Auto Threshold ("Default no-reset");
run ("Set Measurements...", "area mean min integrated limit redirect=None decimal=3");
run("Measure");
```

1.4. Mathematical Model Implementation.

First, the Shapiro-Wilk Normality Test is conducted to check whether the experimental data follows a normality distribution, where σ represents the position parameter, and μ represents the scale parameter (Eqs. 1 and 2). Besides, X_i and Y_i represent the paired variables, consisting of n pairs of observations, and D_i represents the difference of each pair of observations, shown in Eq. 3. The Paired Sample Wilcoxon Signed-Rank test model is based on the non-normality of the difference of the paired X_i & Y_i, rather than the non-normality of X_i or Y_i, respectively.

$$X \sim N(\mu,\sigma^2) \#(1)$$

$$f(x) = \frac{1}{\sigma\sqrt{2\pi}} e^{-\frac{(x-\mu)^2}{2\sigma^2}} \#(2)$$

$$D_i = Y_i - X_i,\ i = 1,2,...,n \#(3)$$

Second, ignoring the sign of the difference, only the absolute value of the difference $|D_i|$ is sorted and the rank r_i is assigned. By re-introducing the symbol of the difference $|D_i|$ to the corresponding rank, two sets of rank are obtained: positive rank and negative rank. The sum of positive rank and negative rank is recorded as W^+ and W^- (Eqs. 4 and 5). The statistic W is defined as the smaller of the two rank sums, namely $W = min(W^+, W^-)$.

$$W^+ = \sum_{i=1}^{n} u_i r_i,\ u_i = \begin{cases} 1, & D_i > 0 \\ 0, & D_i \le 0 \end{cases} \#(4)$$

$$W^- = \sum_{i=1}^{n} v_i r_i,\ v_i = \begin{cases} 1, & D_i < 0 \\ 0, & D_i \ge 0 \end{cases} \#(5)$$

Third, use E to standardize the value of W to get the z score (Eq. 6),

$$z = \frac{W - E(W)}{\sqrt{Var(W)^*}} \#(6)$$

where, $E(W)$ represents the expected value, $Var(W)^*$ reprensents the corrected variance of W, and z can be used to find the standard normal distribution table to determine the p-value of the test. $E(W)$ and $Var(W)^*$ can be acquired using the Eqs. 7, 8 and 9,

$$E(W) = \frac{n(n+1)}{4} \#(7)$$

$$Var(W) = \frac{n(n+1)(2n+1)}{24} \#(8)$$

$$Var(W)^* = Var(W) - \sum_{j=1}^{m} \frac{t_j^3 - t_j}{24} \#(9)$$

where $Var(W)$ denotes the variance of W, t_j is the number of the horizontal rank in group j, and m is the number of the horizontal rank group.

Fourth, test that X_i and Y_i are distributed interchangeably using the signed-rank test statistic (Eq. 10),

$$S = \sum_{i=1}^{n_r} r_i I(D_i > 0) - \frac{n_r(n_r+1)}{4} \#(10)$$

where I is an indicator function that the the difference of i is positive and S denotes the significance.

Finally, the formula for $Cohen's\ d$ in equally sized groups is given by Eqs. 11 and 12,

$$Cohen's\ d = \frac{M_1 - M_2}{S_{pooled}} \#(11)$$

$$S_{pooled} = \frac{\sqrt{S_1^2 + S_2^2}}{2} \#(12)$$

where M_1 and M_2 denote the mean values of X_i and Y_i, respectively and S_{pooled} represents the pooled standard deviations for the two groups. S_1 and S_2 denote the standard deviations of X_i and Y_i.

2. Characterization Result

2.1. XRF Analysis.

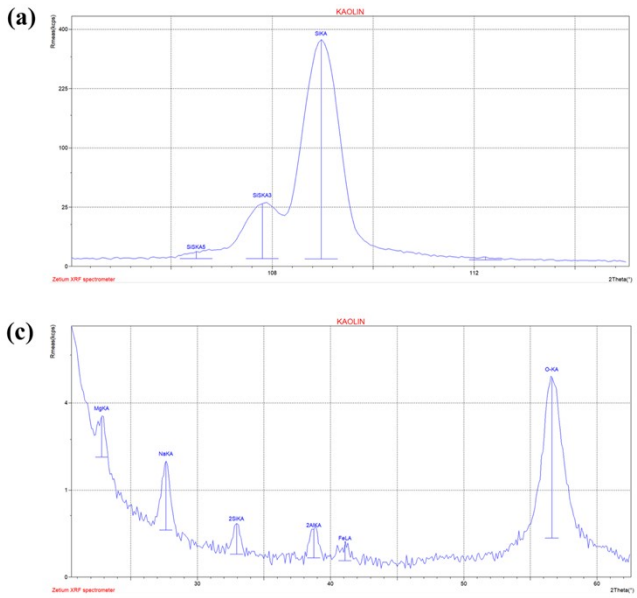

(d)

Oxide	Content (%)
Al_2O_3	48.04
SiO_2	50.02
TiO_2	0.67
Fe_2O_3	0.70
Na_2O	0.31
MgO	0.13
K_2O	0.13

Figure S1. The Content of oxide components of kaolin based on X-ray fluorescence (XRF) spectroscopy analysis. (a-c) XRF spectra. (d) Type and content of oxides in kaolin based on XRF spectrum analysis.

2.2. FT-IR analysis.

As shown in Figure 2b, the characteristic absorption peaks denoting hydroxyl and Si-O in the curcumin/kaolin composites shift from 1116 cm^{-1} and 1032 cm^{-1} to 1109 cm^{-1} and 1021 cm^{-1}, which demonstrates the formation of H-bonds between curcumin and kaolin since when H-bonds form, the stretching vibration frequencies of functional groups involved in hydrogen bonding, such as O-H, typically shift to lower wavenumbers, which has been reported by literatures [7]. The specific explanation is as follows: the formation of hydrogen bonds changes the electron cloud distribution between atoms in the molecule, reducing the bond force constant of the chemical bonds and the molecular vibration frequency [8], and thus causing the absorption peaks of relevant functional groups in the infrared spectrum to shift towards lower wavenumbers, especially in the sensitive fingerprint region [9], Therefore, the results demonstrate the hydrogen bond network structure exists between curcumin and kaolin, which also improves the physical crosslinking inside the composites (Scheme 1).

3. Details of Theoretical Computation.

The ground-state and excited-state geometries were optimized using density functional theory (DFT) and time-dependent density functional theory (TD-DFT) methods, respectively, at the level of B3LYP-D3(BJ)/6-31G*, conducted by Gaussian 16. No symmetry constraint was applied for optimization. The harmonic frequency calculations were performed at the same level as the optimization computation to ensure that all optimized structures have no imaginary frequency. Energies and distributions of the highest occupied molecular orbital (HOMO) and the lowest unoccupied molecular orbital (LUMO) calculations at the level of B3LYP-D3(BJ)/def2-TZVP were

performed to investigate the characteristics of molecular orbits (MOs). The relative energy levels of the ground state (S_0) and the first excited singlet state (S_1) were calculated at the level of PBE0-D3(BJ)/6-31G*. The simulative absorption spectra and PL spectra were performed with Gaussview 6.0 and Origin 2024. Molecular orbit visualization was carried out with the aid of Multiwfn 3.8 and VMD 1.9.4 [10].

4. Reproducibility of the synthesis process across different batches

Figure S2. The synthesized curcumin/kaolin composite powders across batches.

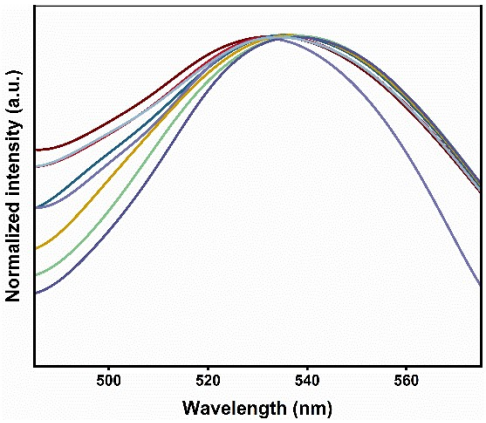

Figure S3. Photoluminescence spectra of the synthesized curcumin/kaolin composites across different batches.

5. Mechanistic study.

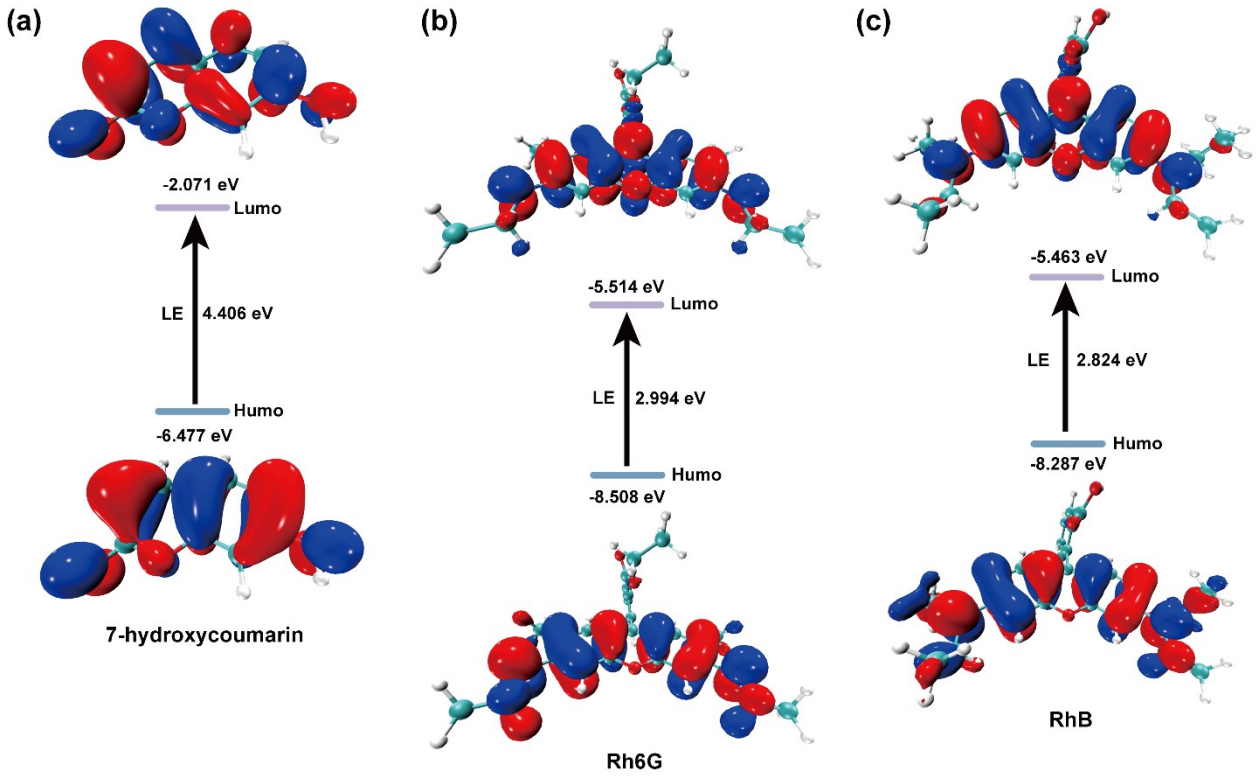

Figure S4. HOMO and LUMO electronic distributions and energies of (a) 7-hydroxycoumarin, (b) Rh6G, and (c) RhB.

For one thing, the absorption peaks show blue shift from Curcumin/Kaolin$_1$ (434 nm), Curcumin/Kaolin$_2$ (430 nm), to Curcumin/Kaolin$_3$ (426 nm) (Figure 4a). For another, the PL emission peaks show blue shift from Curcumin/Kaolin$_1$ (542 nm), Curcumin/Kaolin$_2$ (539 nm), to Curcumin/Kaolin$_3$ (529 nm), either. These results can be ascribed to the slight variations of the optical gaps of Curcumin/Kaolin$_1$, Curcumin/Kaolin$_2$, and Curcumin/Kaolin$_3$. Materials with narrower bandgap tend to absorb longer wavelengths of light, while materials with wider bandgap absorb shorter wavelengths of light. At the same time, the widening of bandgap allows electrons to be excited to higher energy levels, and the fluorescence emitted back to the ground state possesses higher energy, reducing the probability of non-radiative transitions [11]. In addition, a decrease in bandgap indicates that the energy required for electrons to be excited from the valence band to the conduction band is reduced, making it easier for electrons to be excited to the conduction band. When an electron transitions from a low energy level to a high energy level, a redshift phenomenon occurs, that is, a decrease in the bandgap leads to a redshift in the emission wavelength [12].

6. Development of latent fingerprints

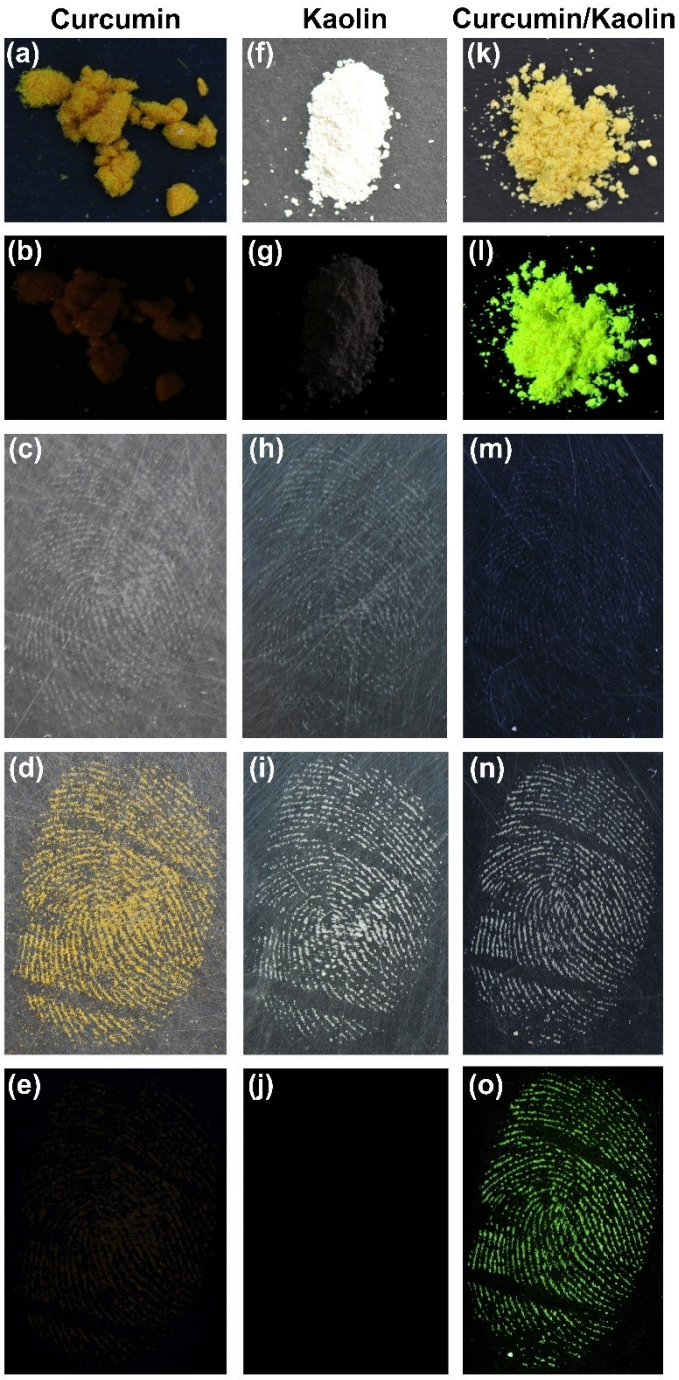

Figure S5 (a-b) curcumin, (f-g) kaolin, (k-l) curcumin/kaolin powders in the natural state and luminescent state. (c), (h), and (m) LFPs left on aluminum sheets. Developed LFPs using (d-e) curcumin, (i-j) kaolin, (n-o) curcumin/kaolin in the natural state and luminescent state.

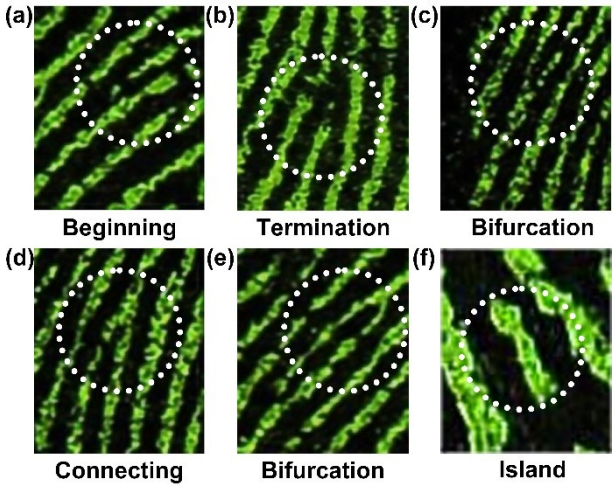

Figure S6. (a) Beginning, (b) termination, (c) bifurcation, (d) connecting, (e) termination, (f) island.

Newly-formed LFPs were first stored at room temperature for 1, 3, 7, 15, 30, and 100 days. Then, these aging LFPs were developed using the curcumin/kaolin powders at the corresponding time points, to test the performance of the synthesized composite powders for the development of aging LFPs.

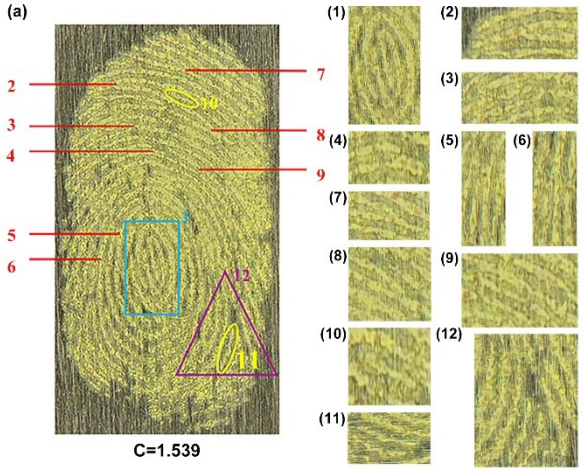

Figure S7. (a) LFP aged for 100d was developed by Curcumin/Kaolin$_2$ powders. (1-12) Detailed features of the developed fingerprint: (1) whorl, (2) bifurcation, (3) connecting, (4) connecting, (5) beginning, (6-8) connecting, (9) intersection, (10-11) islands, and (12) delta.

First, the synthesized powders were stored naturally for 1 month and then used to develop LFPs. Then, the LFPs that had been developed by curcumin/kaolin composites were stored in a sealed refrigerator at room temperature for 1, 3, 5, 7, and 10 days, to investigate the stability of the synthesized powders.

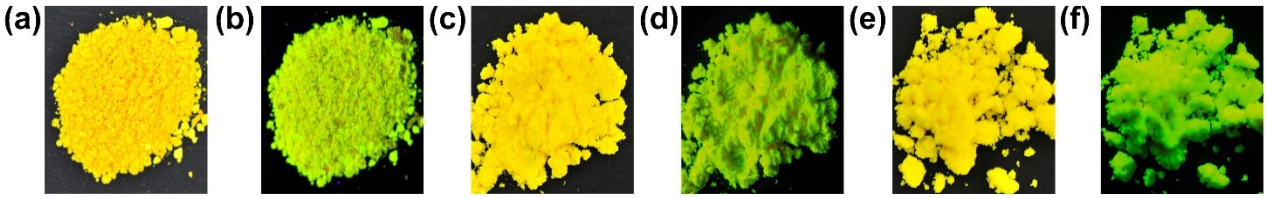

Figure S8. The synthesized curcumin/kaolin powders were stored for 1 month: (a) and (b) Curcumin/Kaolin$_1$, (c) and (d) Curcumin/Kaolin$_2$, and (e) and (f) Curcumin/Kaolin$_3$, in the natural or fluorescent

state, respectively.

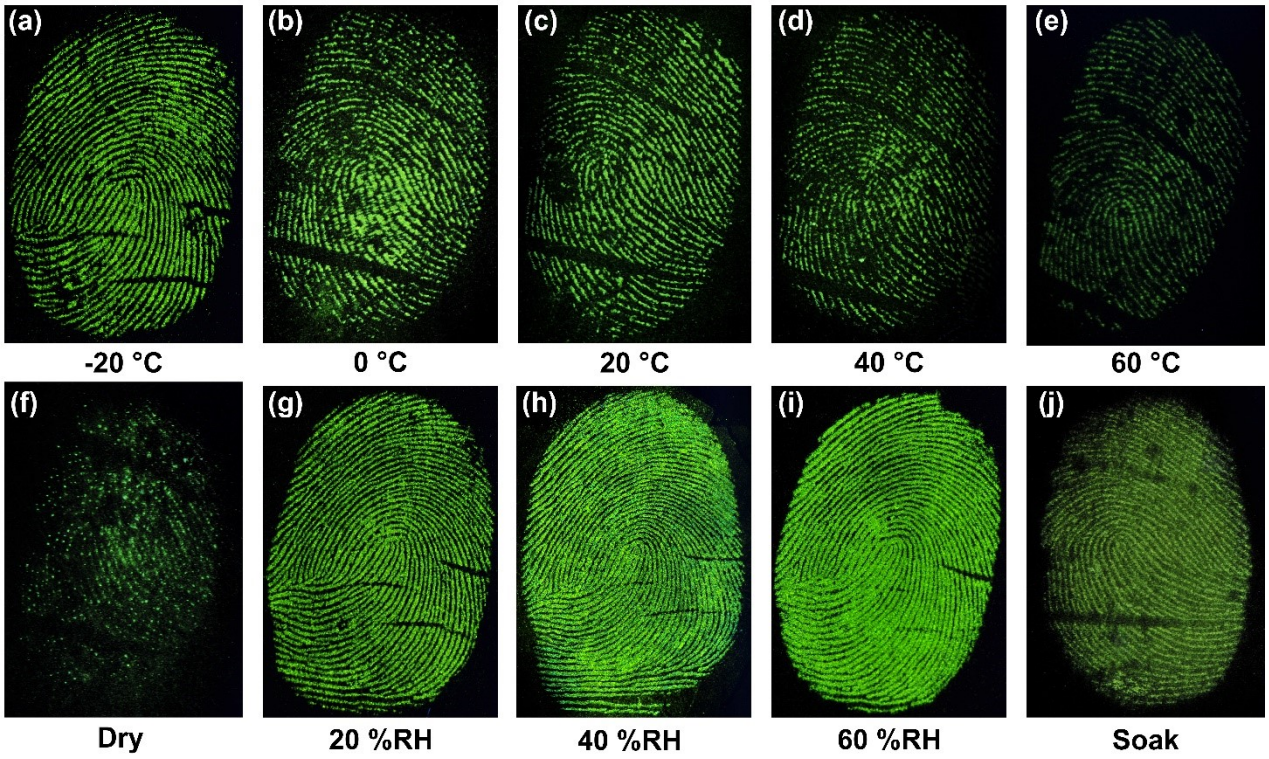

Figure S9. LFPs left in different temperatures and moderate environments were developed with curcumin/kaolin: (a) -20 °C, (b) 0 °C, (c) 20 °C, (d) 40 °C, (e) 60 °C, (g) 20 %RH, (h) 40 %RH, (i) 60 %RH. (f) and (j) represents LFPs were dried in an oven overnight and soaked in water.

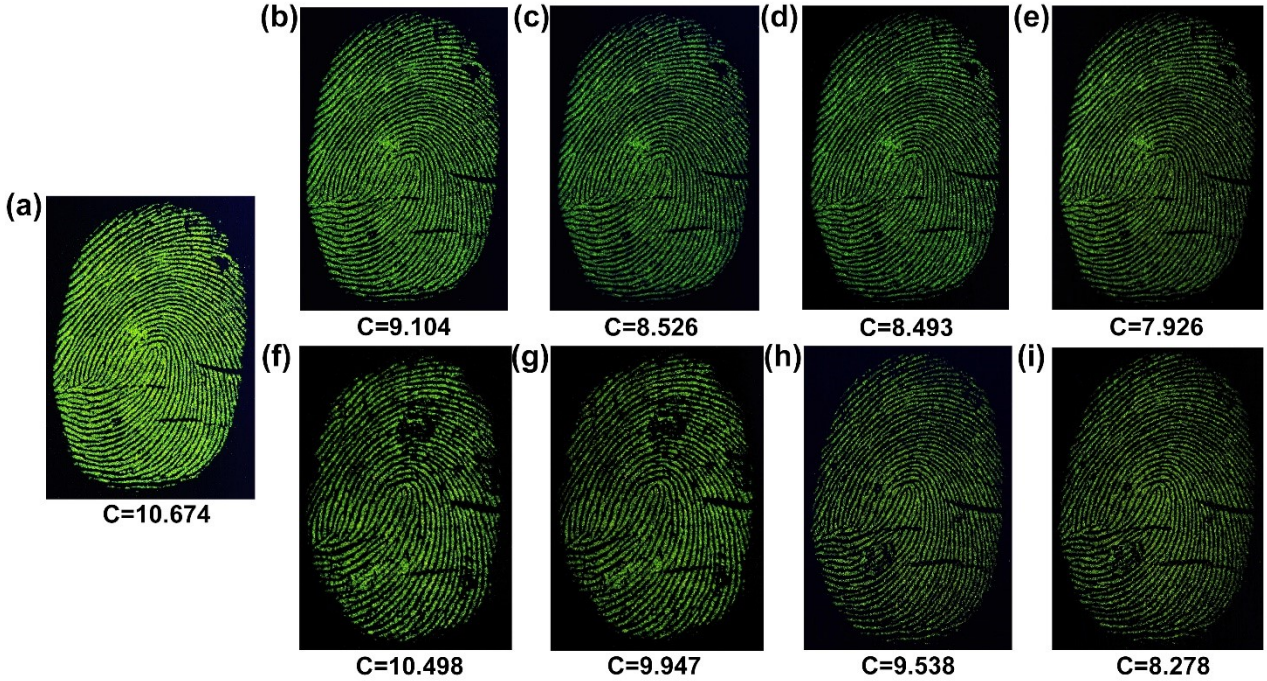

Figure S10. LFPs left on brass plates were developed by curcumin/kaolin powders that were aged for 1 month. After being developed and then stored for different times, LFPs were photographed to investigate the stability of the synthesized powders in developing LFPs. (a) 0d, (b) 3d, (c) 5d, (d) 7d, and (e) 10d of Curcumin/Kaolin$_3$. (f) 3d, and (g) 7d of Curcumin/Kaolin$_2$. (h) 3d, and (i) 5d of Curcumin/Kaolin$_1$.

7. Quantification of Fingerprint Fluorescence Contrast

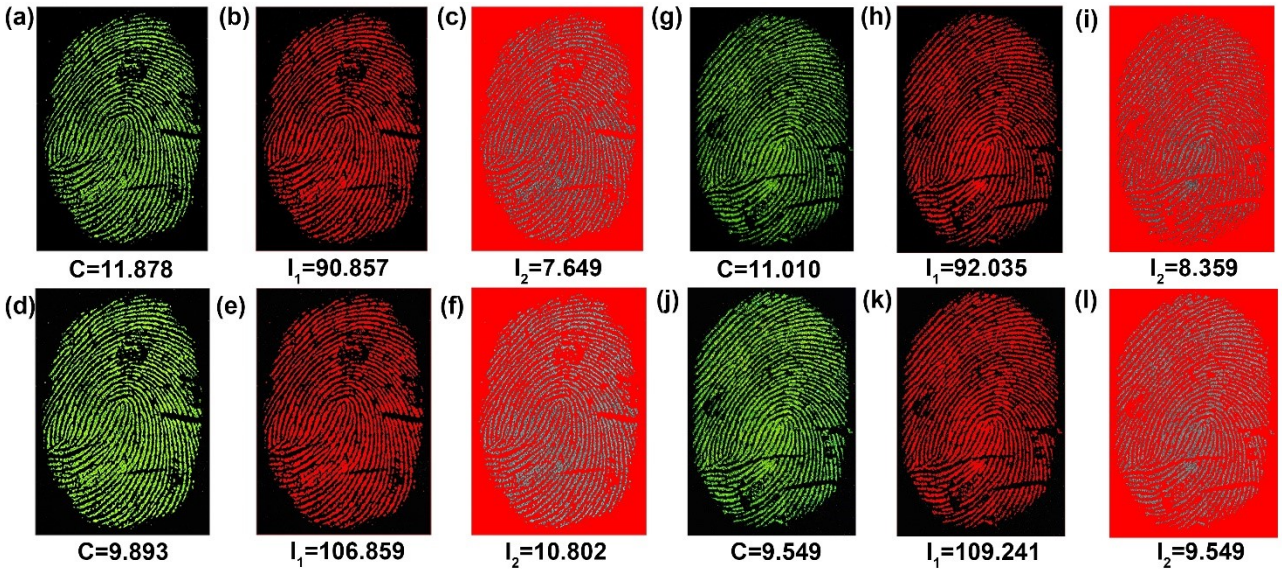

Figure S11. LFPs were developed by Curcumin/Kaolin$_2$. And C, I_1, and I_2 represent the developed contrast, fluorescence intensity of the fingerprint area and the background area, respectively, with the gray value serving as the metric. The same developed LFP left on brass was photographed under (a) ISO 500 and (d) ISO 800 settings. Likewise, the same developed LFP left on aluminum was photographed under (g) ISO 500 and (j) ISO 800 settings. (b), (e), (h), and (k) represent the fingerprint area of each LFP, based on the grayscale threshold segmentation. Similarly, (c), (f), (h), and (k) denote the segmented background area of each LFP.

8. Comparison between FFIR quantification and qualitative evaluations

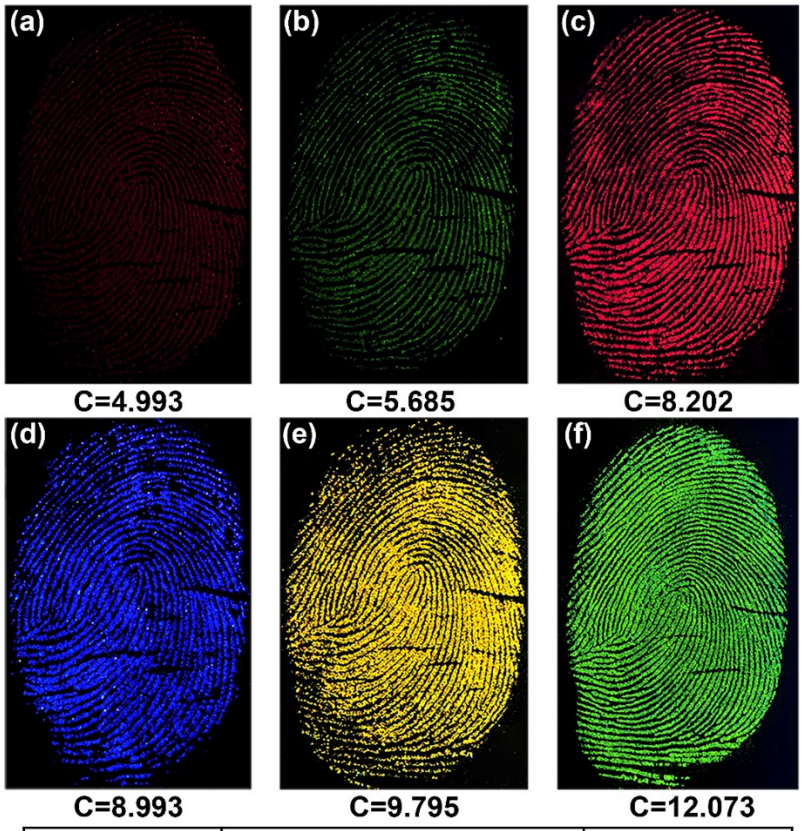

LFPs	Qualitative evaluation			Quantification
	High	Low	Rank	Contrast
a	0	20	6	4.993
b	0	20	5	5.685
c	18	2	3 (14), 4 (6)	8.202
d	15	5	3 (6), 4 (14)	8.993
e	20	0	1 (9), 2 (11)	9.795
f	20	0	1 (11), 2 (9)	12.073

Figure S12. Comparison between FFIR quantification and qualitative evaluations by forensic professionals.

9. Channel Separation for Grayscale Image Enhancement

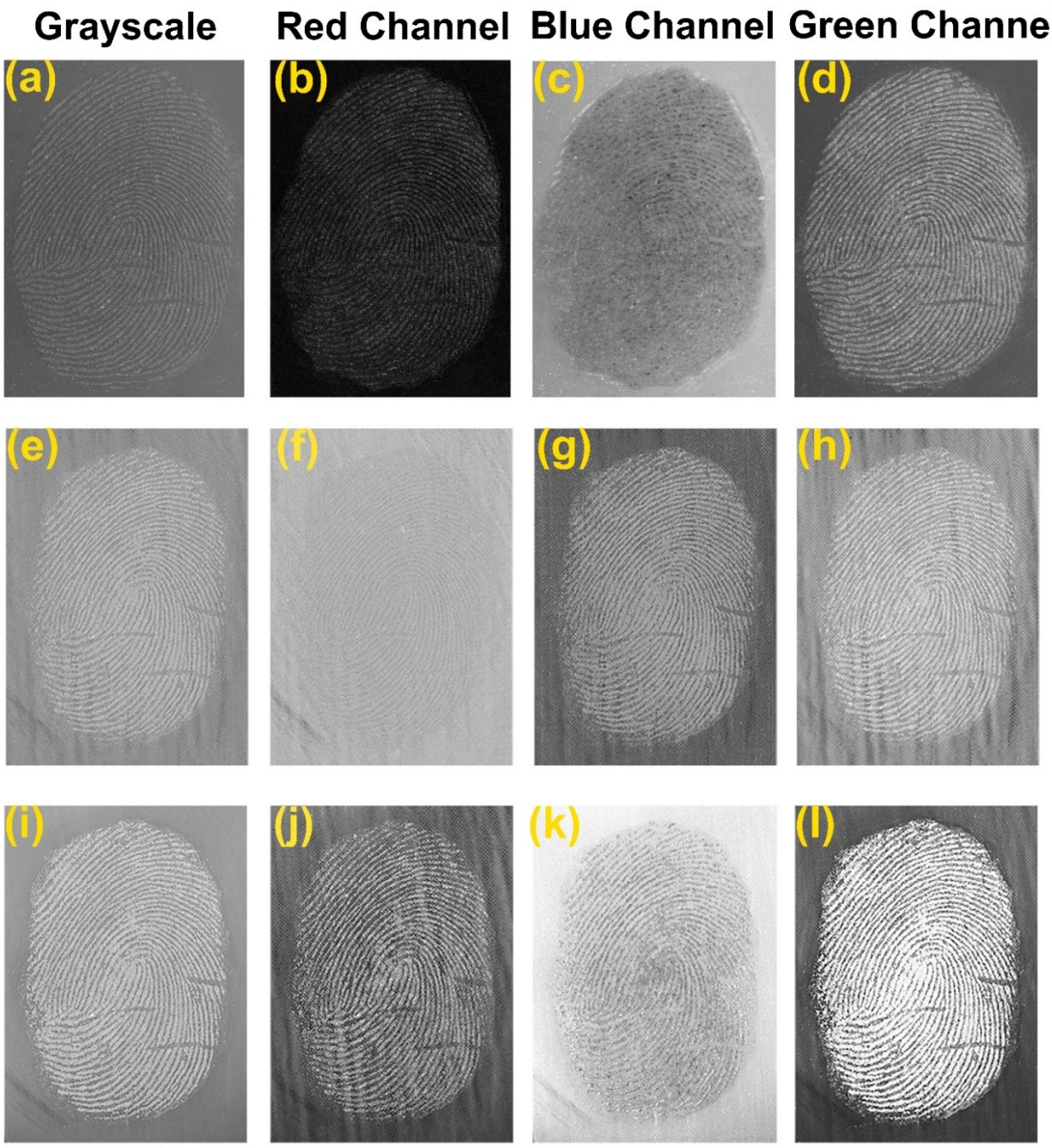

Figure S13. LFPs left on (a) transparent plastic sheet and (e) and (i) leather developed by Curcumin/Kaolin composite powders. Images in columns from left to right: grayscale images of the developed fingerprints in the luminescent mode; and red, blue, and green channel images separated from the fluorescent images.

10. Tunable and Multi-Color Fingerprint Image Enhancement

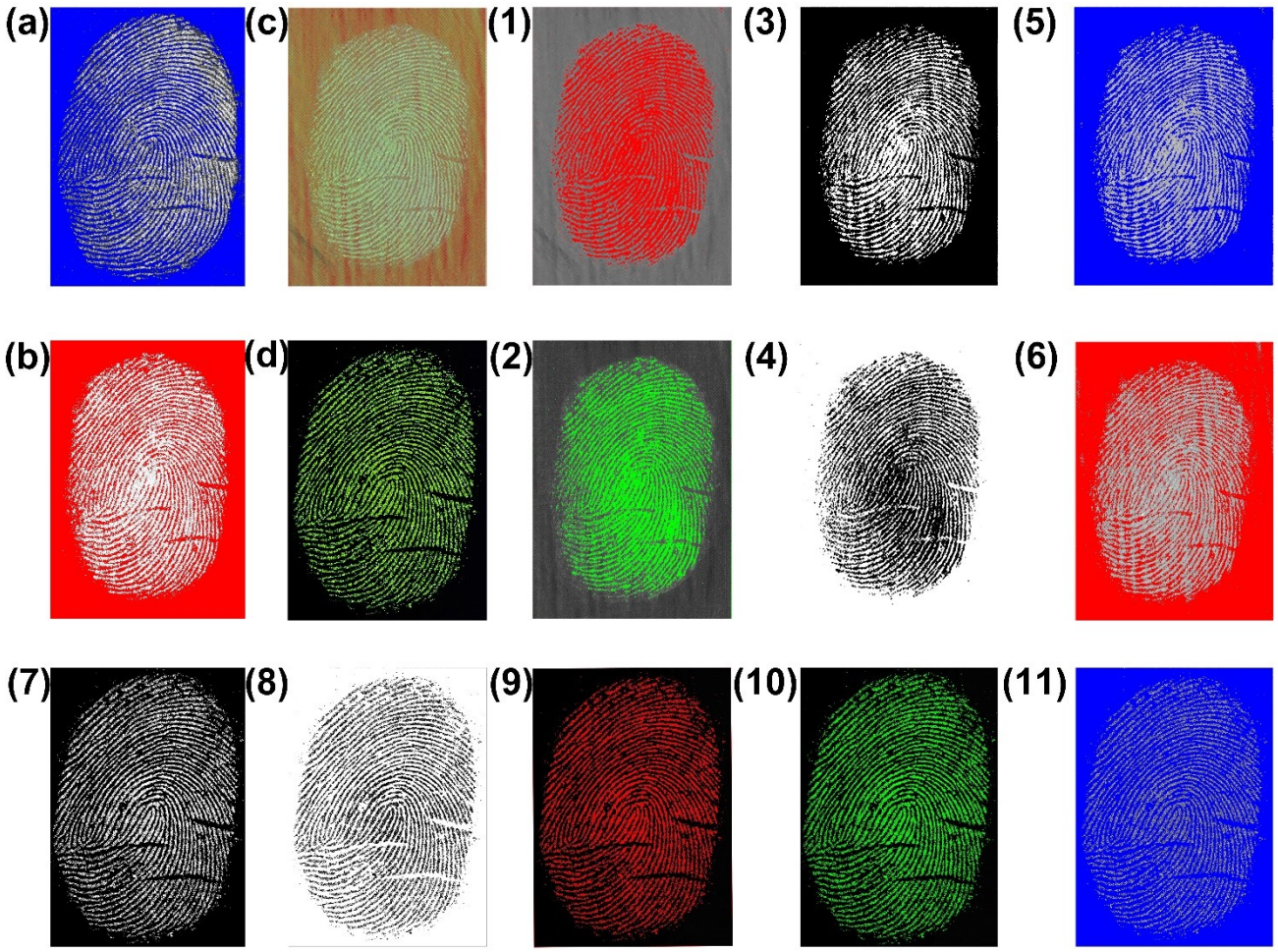

Figure S14. (a) and (b) Additional enhanced images of Figure 8(0) and (6), respectively. LFPs imprinted on (c) leather with intense background pattern interference and (d) brass plate with negligible background interference were developed by curcumin/kaolin composites in the natural mode and the luminescent mode, respectively. (1)-(6) and (7)-(11) Tunable and multi-color enhanced images via FFIR of (c) and (d), respectively.

11. Mathematical Model-Based FFIR Method Validation.

The descriptive statistics and the normality test based on the S-W Test were performed to obtain an intuitive overview of the acquired data and to determine whether the data conforms to the normal distribution. Then, the Paired Sample Wilcoxon Signed-Rank Test model was established to validate the sensitivity of the developed FFIR method in tracking image capture parameters.

The results of descriptive statistics show that the average value of the ISO 500 group data is 7.314, and the average value of the ISO 800 group data is 6.522. From the previous contrast quantification results, it can be noticed that some LFPs even cannot be directly observed with the naked eye. Consequently, the LFPs in PL mode are conducive to effective visualization and contrast differentiation. For ISO 500, the skewness is close to 0, and the kurtosis is slightly less than 0, suggesting that the distribution pattern is relatively symmetrical and may be slightly flat. For ISO 800, the skewness value is slightly less than 0, and the kurtosis value is also less than 0, indicating that the distribution may be slightly left-skewed and relatively flat. Moreover, the results of the S-W normality test indicate that the "P" -values of the ISO 500 and ISO 800 groups are 0.074 and 0.130, respectively, which indicates that the two single-group datasets follow the normal distribution. The P-P and Q-Q

diagrams of the two groups indicate a good fit between the observed and predictive values, thereby confirming the normality of the two sets of data.

12. Effect comparison between FFIR and existing methods.

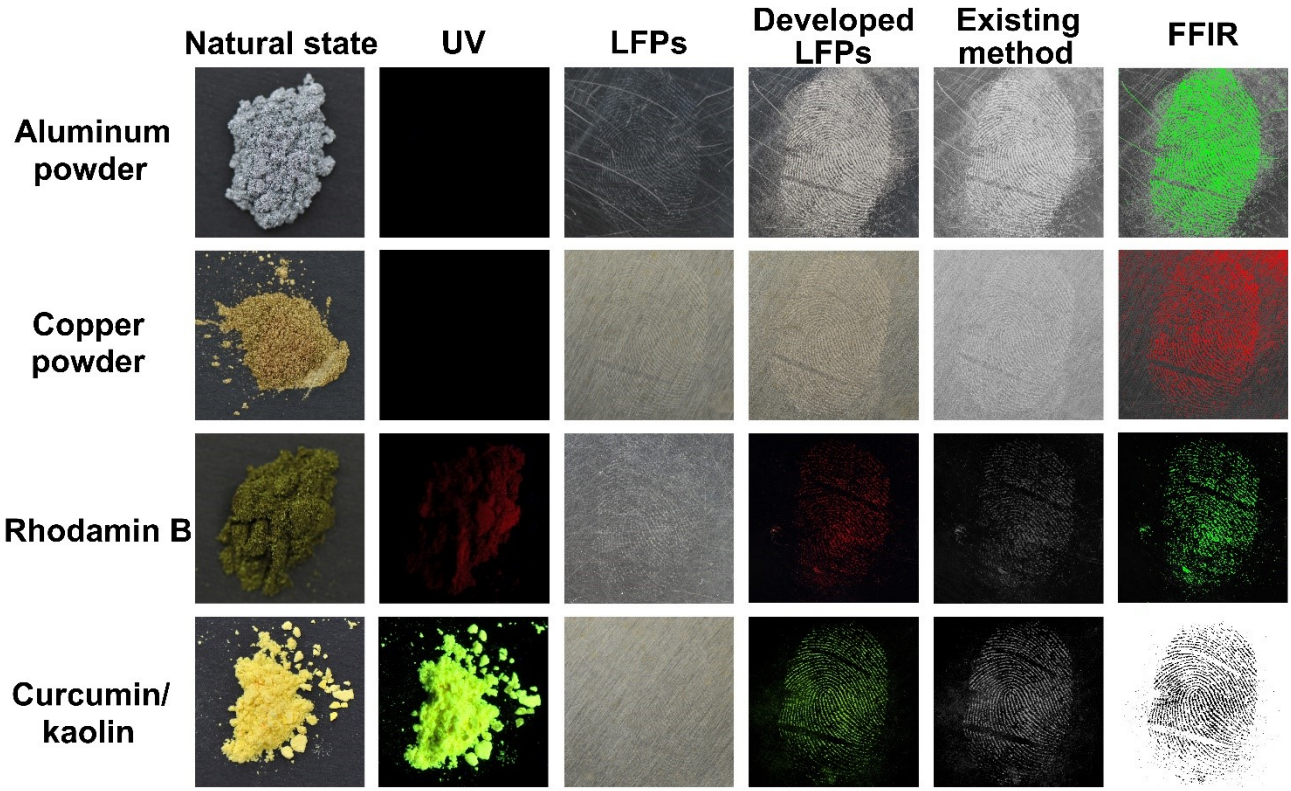

Figure S15 Effect comparison between FFIR and existing fingerprint development and enhancement methods.

References

[1] M. Wang, D. Shen, Z. Zhu, J. Ju, J. Wu, Y. Zhu, M. Li, C. Yuan, C. Mao, Dual-mode fluorescent development of latent fingerprints using NaYbF4:Tm upconversion nanomaterials, Mater. Today Adv. 8 (2020) 100113. https://doi.org/https://doi.org/10.1016/j.mtadv.2020.100113.

[2] Y. Lou, X. Zhou, D. Zhang, F. Cheng, Microrheological Phenomenon and Mechanical Properties of High-Aspect-Ratio Microgroove Injection Moulding of Kaolin/PP Composites, Int. J. Mol. Sci. 23(9) (2022). https://doi.org/10.3390/ijms23094944.

[3] A.H. Jawad, A.S. Abdulhameed, E. Kashi, Z.M. Yaseen, Z.A. Alothman, M.R. Khan, Cross-Linked Chitosan-Glyoxal/Kaolin Clay Composite: Parametric Optimization for Color Removal and COD Reduction of Remazol Brilliant Blue R Dye, J. Polym. Environ. 30(1) (2022) 164-178. https://doi.org/10.1007/s10924-021-02188-1.

[4] P. Liczbiński, J. Michałowicz, B. Bukowska, Molecular mechanism of curcumin action in signaling pathways: Review of the latest research, Phytother. Res. 34(8) (2020) 1992-2005. https://doi.org/https://doi.org/10.1002/ptr.6663.

[5] S.R. Shirsath, A.P. Patil, B.A. Bhanvase, S.H. Sonawane, Ultrasonically prepared poly(acrylamide)-kaolin composite hydrogel for removal of crystal violet dye from wastewater, J. Environ. Chem. Eng. 3(2) (2015) 1152-1162. https://doi.org/10.1016/j.jece.2015.04.016.

[6] Z. Cao, Q. Wang, H. Cheng, Recent advances in kaolinite-based material for photocatalysts, Chin. Chem. Lett. 32(9) (2021) 2617-2628. https://doi.org/https://doi.org/10.1016/j.cclet.2021.01.009.

[7] W. Yuan, J. Zhou, M. Jiang, Q. Sun, G. Ye, X. Zhang, H. Bi, Latent fingerprints identification and ink-free printing of

fluorescent lignin-derived CDs/PVA nanocomposite with multi-stimuli responsive shape memory behavior, Ind. Crops Prod. 205 (2023) 117563. https://doi.org/https://doi.org/10.1016/j.indcrop.2023.117563.

[8] N.M. Atakishiyev, A.U. Klimyk, K.B. Wolf, A discrete quantum model of the harmonic oscillator, J. Phys. A: Math. Theor. 41(8) (2008) 085201. https://doi.org/10.1088/1751-8113/41/8/085201.

[9] J. Coates, Interpretation of Infrared Spectra, A Practical Approach, Encyclopedia of Analytical Chemistry. https://doi.org/https://doi.org/10.1002/9780470027318.a5606.

[10] T. Lu, F. Chen, Multiwfn: A multifunctional wavefunction analyzer, J. Comput. Chem. 33(5) (2012) 580-592. https://doi.org/https://doi.org/10.1002/jcc.22885.

[11] C. Siu, Semiconductor Physics, in: C. Siu (Ed.), Electronic Devices, Circuits, and Applications, Springer International Publishing, Cham, 2022, pp. 35-39. https://doi.org/10.1007/978-3-030-80538-8_3.

[12] J. Wang, D. Li, Research progress in visualization of LFPs based on nano fluorescent carbon dots, Mater. Rep. 39(9) (2025) 24020140 (in Chinese). https://doi.org/10.11896/cldb.24020140.